Supporting Information of

Highly [001]-Oriented N-doped Orthorhombic Nb_2O_5 Microflowers with Intercalation Pseudocapacitance for Lithium-ion Storage

Guangyin Liu,[a] Shanshan Liu,[a] Hao Chen,[a] Xiaodi Liu,[a]* Xinwei Luo,[a] Xiu Li,[b]* and Jianmin Ma[b]

[a] *College of Chemistry and Pharmaceutical Engineering, Nanyang Normal University, Nanyang 473061, China*

[b] *School of Materials and Energy, University of Electronic Science and Technology of China, Chengdu 611731, China*

*Corresponding author: E-mail: liuxiaodiny@126.com (X. Liu); x.li@uestc.edu.cn (X. Li).

Structural characterization and electrochemical measurements of N-doped orthorhombic Nb_2O_5 microflowers (N-Nb_2O_5) and orthorhombic Nb_2O_5 microspheres (Nb_2O_5-MS):

The crystal structures of Nb_2O_5-MS and N-Nb_2O_5 are recorded in the range of 10-70° (2θ) on a X-ray diffractometer (XRD, Rigaku D/max-2500) using Cu Kα radiation. The morphologies and nanostructures of samples are tested by scanning electron microscopy (SEM, ZEISS sigma-500), transmission electron microscopy (TEM, JEM-2100F), and high-resolution transmission electron microscopy (HRTEM, JEM-2100F). The special BET surface areas of samples are examined by N_2 adsorption-desorption isotherms at 77 K on a Micromeritics Autosorb-iQ apparatus. X-ray photoelectron spectra (XPS) are performed by Thermo ESCALAB 250XI electron spectrometer (Al Kα). The binding energies of the peaks are calibrated by setting the adventitious C 1s peak at a fixed value of 284.5 eV and fitted by the XPSPEAK41 fitting software. UV-Vis diffuse reflectance spectra (DRS) of the samples in the wavelength range of 300-750 cm^{-1} are recorded on a UV-vis spectrophotometer (Hitachi U-3010), using $BaSO_4$ as the background.

The active anodic materials (Nb_2O_5-MS and N-Nb_2O_5), acetylene black, and polyvinylidene fluoride with a ratio of 70:20:10 wt% are mixed in N-methyl-2-pyrrolidone. Then, the slurry is uniformly coated on Cu foils and dried in vacuum (120 °C, 12 h). Subsequently, the electrodes are assembled into CR2025 coin-type cells in an Argon-filled glove box. Li is served as the counter and reference electrode. The loading amount of the electrode is about 2.0 mg cm^{-2}. The electrolyte is 1 mol L^{-1} $LiPF_6$ in ethylene carbonate, ethyl methyl carbonate, and diethyl carbonate (1:1:1 vol%). Galvanostatic measurements are evaluated by a LAND CT2001A battery tester. Cyclic voltammetry (CV) measurements are carried out on a CHI660D Electrochemical Workstation. Electrochemical impedance spectroscopy (EIS) tests are performed on a Solatron 1260 Impedance Analyzer with potentiostatic signal amplitude of 10 mV.

Tab. S1. The crystal lattice parameters of Nb_2O_5-MS and N-Nb_2O_5.

Samples	*a* (Å)	*b* (Å)	*c* (Å)	*V* (Å^3)
Nb_2O_5-MS	6.1702	29. 1645	3.9014	702.74
N-Nb_2O_5	6.1752	29. 2092	3.9288	708.64

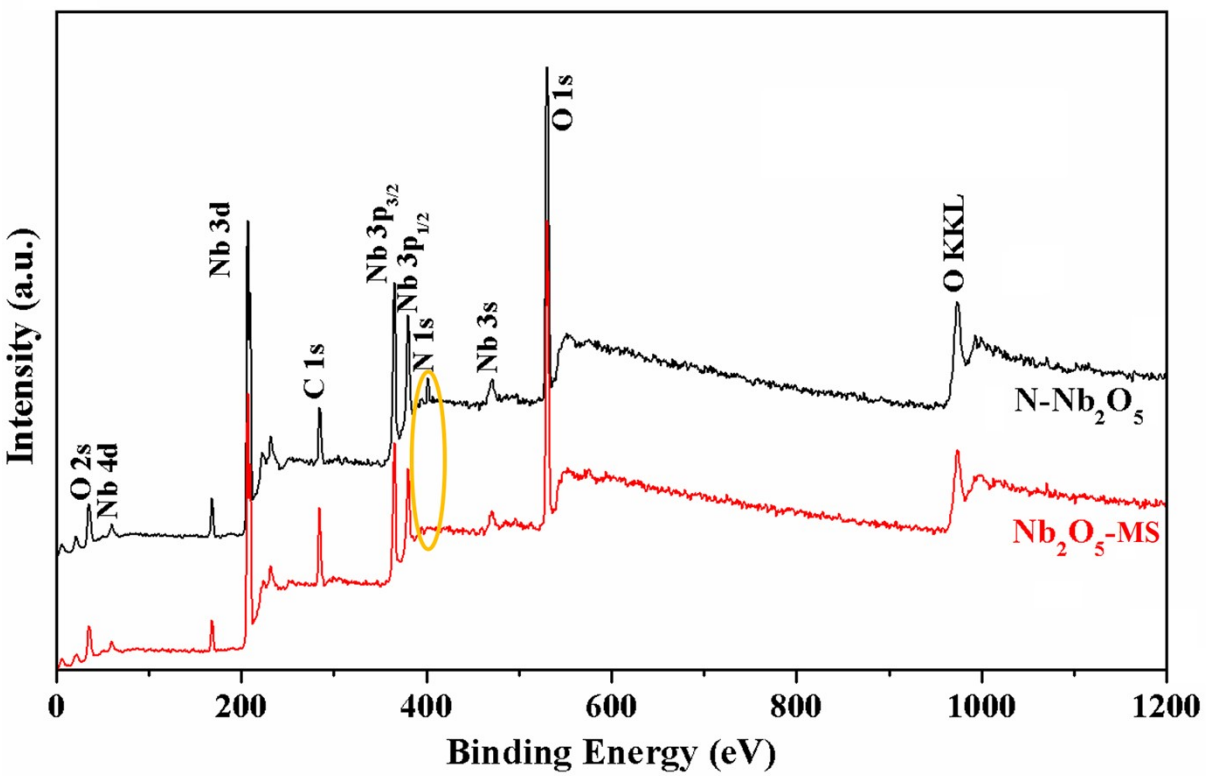

Fig. S1. XPS spectra of N-Nb_2O_5 and Nb_2O_5-MS.

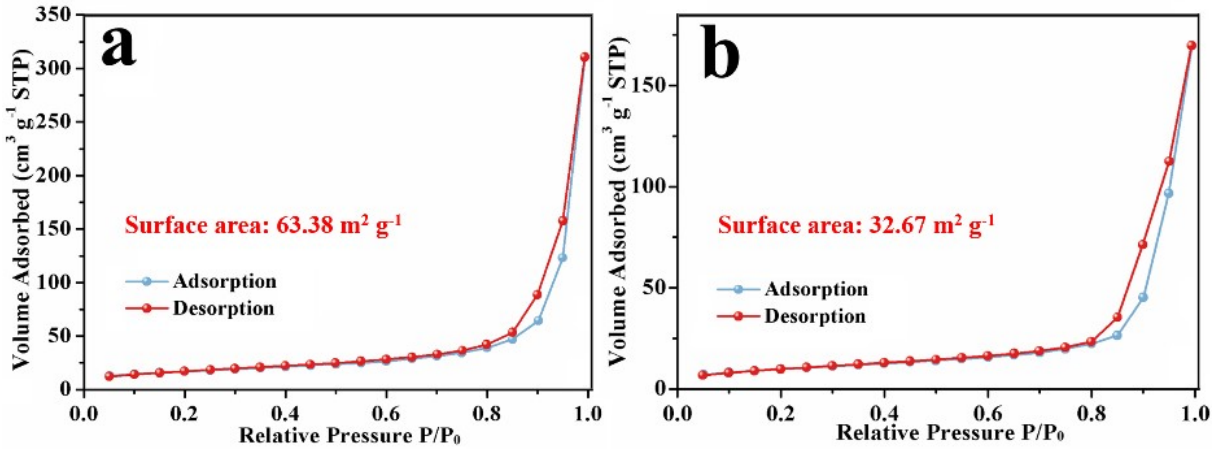

Fig. S2. Nitrogen adsorption-desorption isotherms of (a) N-Nb_2O_5 and (b) Nb_2O_5-MS.

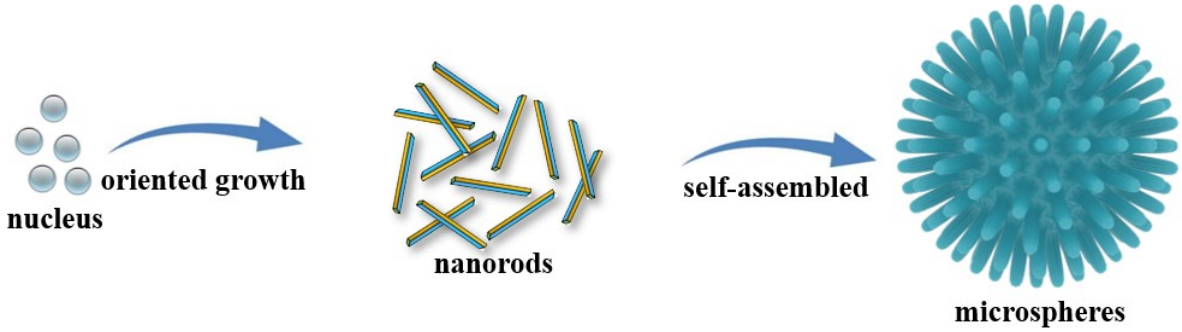

Fig. S3. The possible formation process of Nb_2O_5-MS.

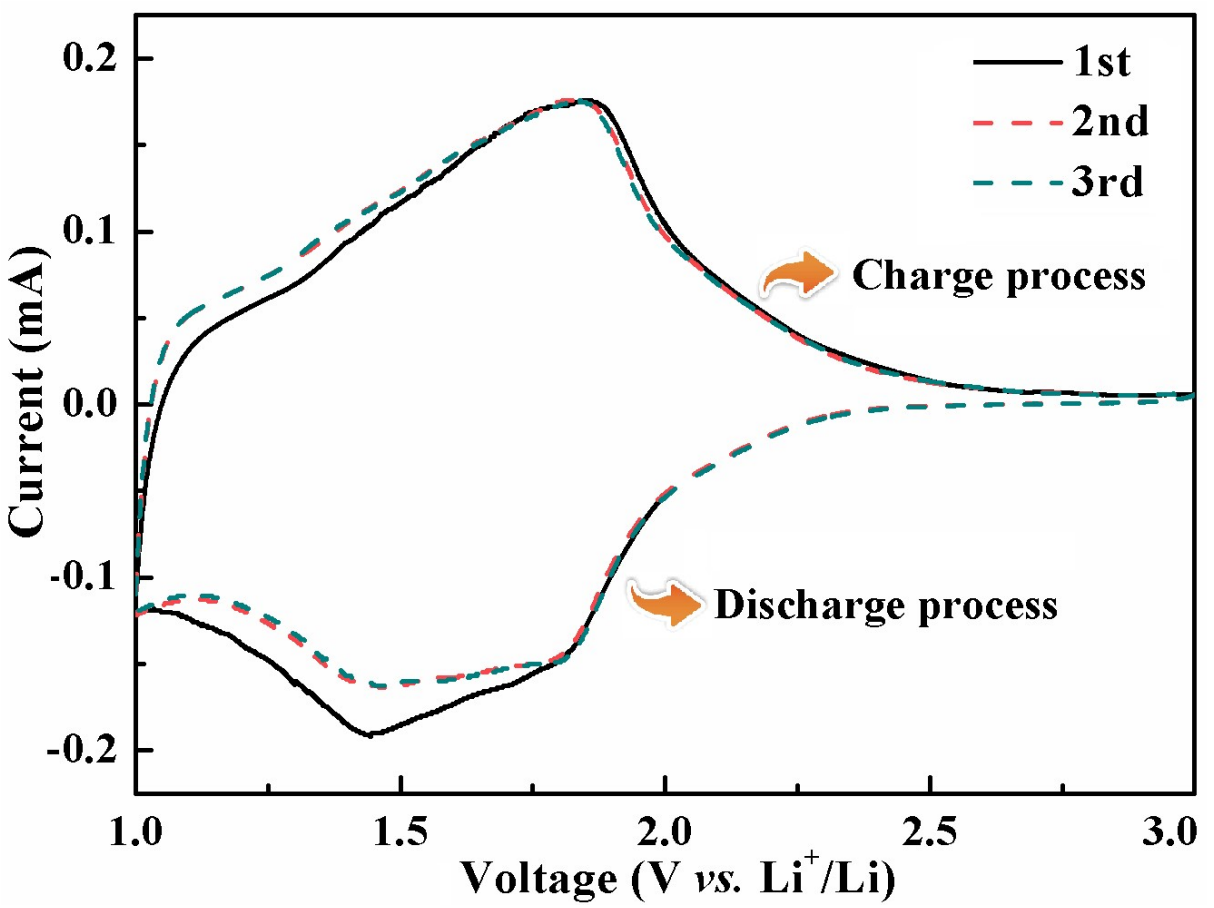

Fig. S4. The initial three CV curves of N-Nb_2O_5 in a voltage range of 1.0-3.0 V (*vs.* Li/Li^+) at a scan rate of 0.1 mV s^{-1}.

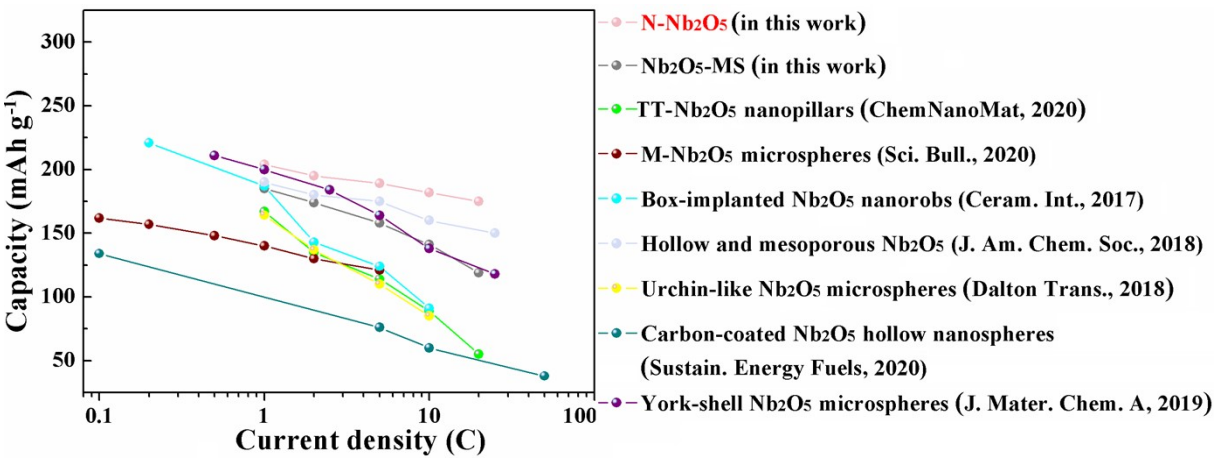

Fig. S5. The comparison of the rate capabilities between the obtained N-Nb_2O_5, Nb_2O_5-MS, and other previously reported Nb_2O_5-based anodes.

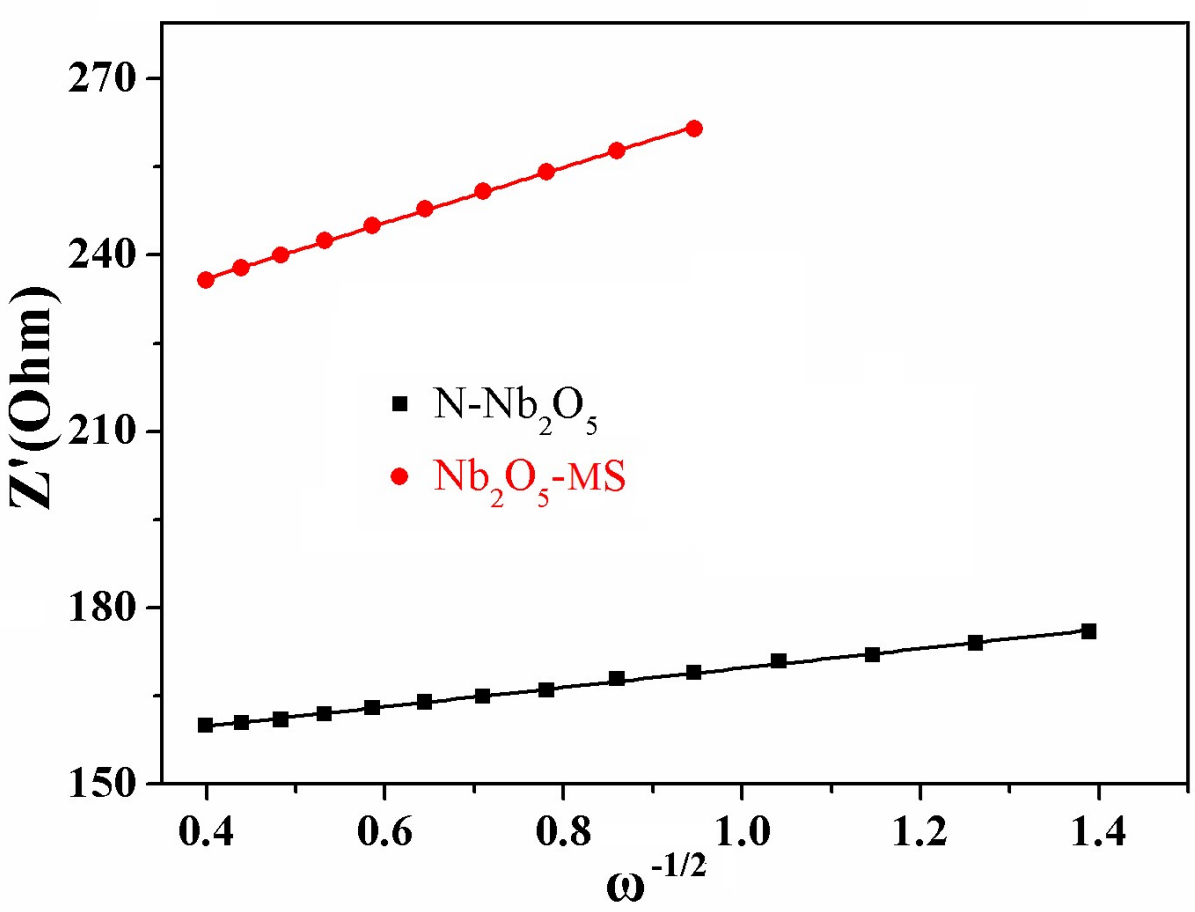

Fig. S6. Relationship between imaginary resistance (Z') and inverse square root of angular speed ($\omega^{-0.5}$) at low frequency region.

Based on the slopes of the Z'-$\omega^{-0.5}$ plots (Fig. S5), the σ value of Nb_2O_5-MS is larger than that of N-Nb_2O_5, so the calculated Li^+ ions diffusion coefficient of Nb_2O_5-MS is smaller than that of N-Nb_2O_5.

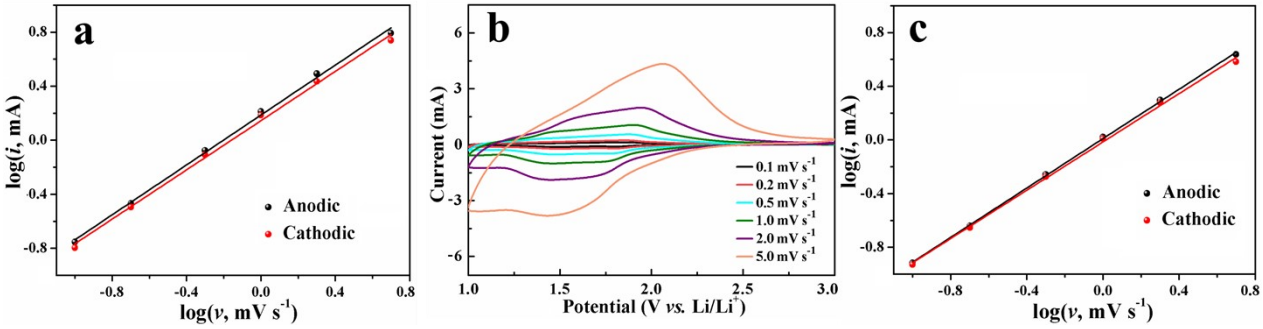

Fig. S7. (a) Plots of log(*i*) *vs.* log(*v*) used to calculate *b*-values of N-Nb_2O_5; (b) cyclic voltammograms of Nb_2O_5-MS at different scanning rates with potential window of 1.0-3.0 V *vs.* Li/Li^+; (b) plots of log(*i*) *vs.* log(*v*) used to calculate *b*-values of Nb_2O_5-MS.

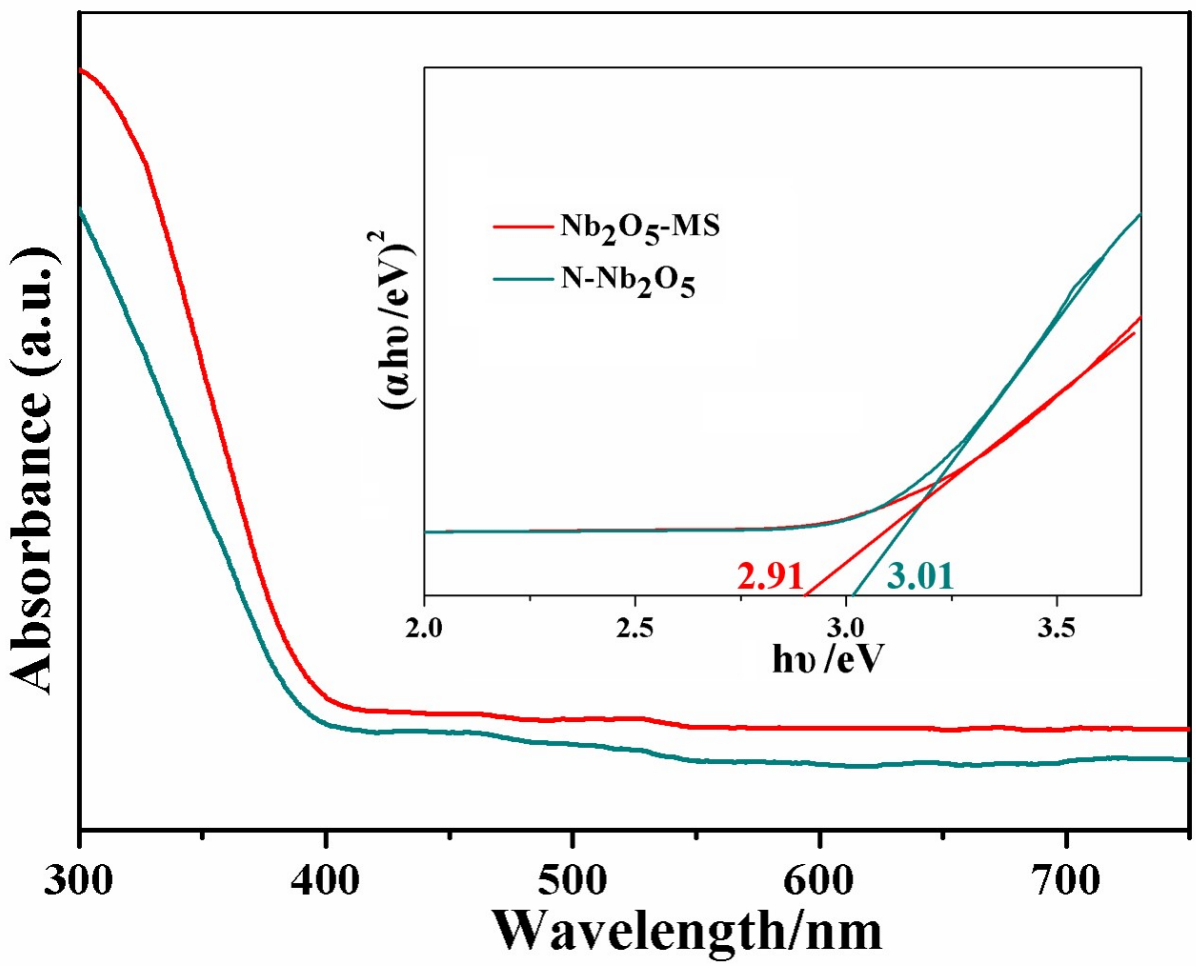

Fig. S8. UV-Vis diffuse reflectance spectra and the corresponding Tauc's curves of N-Nb_2O_5 and Nb_2O_5-MS.

Tab. S2. Electrochemical performance of full cells with Nb-based anodes

Full cell systems	Discharge capacity	Cyclability	Ref.
$LiNi_{0.5}Mn_{0.3}Co_{0.2}O_4$||N-$Nb_2O_5$	232.8 mAh g^{-1} (1 C) 141.3 mAh g^{-1} (10 C)	126.2 mAh g^{-1} (3500 cycles, 10 C)	This work
$LiNi_{0.5}Mn_{0.3}Co_{0.2}O_4$||$Al_{0.5}Nb_{24.5}O_{62}$	143 mAh g^{-1} (1 C) 78 mAh g^{-1} (10 C)	69.6 mAh g^{-1} (800 cycles, 10 C)	1
$LiMn_2O_4$//$MoNb_6O_{18}$	196.3 mAh g^{-1} (0.2 C)	152 mAh g^{-1} (30 cycles, 0.2 C)	2
$LiNi_{0.5}Mn_{1.5}O_4$||$HfNb_{24}O_{62}$	213 mAh g^{-1} (0.1 C) 78 mAh g^{-1} (10 C)	~75 mAh g^{-1} (500 cycles, 5 C)	3
$LiFePO_4$||$TiNb_2O_7$	198.1 mAh g^{-1} (1 A g^{-1}) 127.8 mAh g^{-1} (5 A g^{-1})	131.2 mAh g^{-1} (2000 cycles, 2 A g^{-1})	4
$LiNi_{0.5}Mn_{1.5}O_4$||$Zn_2Nb_{34}O_{87}$-N	236 mAh g^{-1} (0.1 C)	97.8 mAh g^{-1} (1000 cycles, 5 C)	5
$LiMn_2O_4$||$MoNb_{12}O_{33}$	234 mAh g^{-1} (0.1 C) 95 mAh g^{-1} (10 C)	108.9 mAh g^{-1} (1000 cycles, 5 C)	6
$LiMn_2O_4$||$V_3Nb_{17}O_{50}$	102 mAh g^{-1} (1 C) 61 mAh g^{-1} (10 C)	62.6 mAh g^{-1} (500 cycles, 5 C)	7
$LiMn_2O_4$||IO-$Cu_2Nb_{34}O_{87}$	229 mAh g^{-1} (0.1 C) 106 mAh g^{-1} (10 C)	99.3 mAh g^{-1} (500 cycles, 10 C)	8
$LiNi_{0.5}Mn_{0.3}Co_{0.2}O_2$||$T_{i2}Nb_{10}O_{29}$@F-C	196 mAh g^{-1} (1 C) 111 mAh g^{-1} (10 C)	70 mAh g^{-1} (500 cycles, 10 C)	9

[1] Q. Fu, R. Li, X. Zhu, G. Liang, L. Luo, Y. Chen, C. Lin, X.S. Zhao, Design, synthesis and lithium-ion storage capability of $Al_{0.5}Nb_{24.5}O_{62}$, J. Mater. Chem. A, 2019, 7, 19862-19871.

[2] J. Cheng, F. Lu, X. Kuang, Shear-structured $MoNb_6O_{18}$ as a new anode for lithium-ion batteries, Mater. Adv., 2021, 2, 6272-6277.

[3] Q. Fu, H. Cao, G. Liang, L. Luo, Y. Chen, V. Murugadoss, S. Wu, T. Ding, C. Lin, Z. Guo, A highly Li^+-conductive $HfNb_{24}O_{62}$ anode material for superior Li^+ storage, Chem. Commun., 2020, 56, 619-622.

[4] L. Yu, J. Lv, Z. Zhou, Y. Li, M. Wei, Hierarchical structure $TiNb_2O_7$ microspheres derived from titanate for high-performance lithium-ion batteries, CrystEngComm, 2021, 23, 4905-4909.

[5] X. Zhu, H. Cao, R. Li, Q. Fu, G. Liang, Y. Chen, L. Luo, C. Lin, X.S. Zhao, Zinc niobate materials: crystal structures, energy-storage capabilities and working mechanisms, J. Mater. Chem. A, 2019, 7, 25537-25547.

[6] X. Zhu, J. Xu, Y. Luo, Q. Fu, G. Liang, L. Luo, Y. Chen, C. Lin, X.Z. Zhao, $MoNb_{12}O_{33}$ as a new anode material for high-capacity, safe, rapid and durable Li^+ storage: structural characteristics, electrochemical properties and working mechanisms, J. Mater. Chem. A, 2019, 7, 6522-6532.

[7] Q. Fu, X. Zhu, R. Li, G. Liang, L. Luo, Y. Chen, Y. Ding, C. Lin, K. Wang, X.S. Zhao, A low-strain $V_3Nb_{17}O_{50}$ anode compound for superior Li^+ storage, Energy Storage Mater. 2020, 30, 401-411.

[8] X. Zhu, G. Liang, Q. Fu, R. Li, Y. Chen, Y. Bi, D. Pan, R. Das, C. Lin, Z. Guo, An inverse opal $Cu_2Nb_{34}O_{87}$ anode for high-performance Li^+ storage, Chem. Commun., 2020, 56, 7321-7324.

[9] X. Ji, Y. Yang, Y. Ding, Z. Lu, G. Liu, Y. Liu, J. Song, Z. Yang, X. Liu, Fluorine-doped carbon-coated mesoporous $Ti_2Nb_{10}O_{29}$ microspheres as a high-performance anode for lithium-ion batteries, J. Phys. Chem. C, 2022, 126, 7799-7808.